Proceedings World Geothermal Congress 2026
Calgary, Canada, June 8 – 11, 2026

CFD Model of Two-phase Flow Geothermal Fluid Through an Orifice Plate

Mohamad Husni Mubarok[1]*, Ahmad Yani[2], Andi Joko Nugroho[3]
Operation Directorate, PT Pertamina Geothermal Energy Tak, Jakarta 10110, Indonesia[1*, 2, 3]
husnimubarok@pertamina.com

Keywords: Computational fluid dynamics, Two-phase flow, Geothermal fluids, Orifice plate, Pressure drop, Pressure profile, Velocity, Discharge coefficient

ABSTRACT

This paper presents a computational fluid dynamics (CFD) model for simulating the two-phase flow of geothermal fluids through a sharp-edge orifice plate, focusing on the pressure drop and flow characteristics during measurement. The numerical simulations were conducted using the ANSYS Fluent solver, and the results were validated with experimental data from a geothermal well. A mixture method was employed to simulate the combination of steam and liquid phases typically found in geothermal wells. The study explores the CFD model setup, including the selection of appropriate turbulence and phase interaction models, and presents detailed results of the pressure profile, velocity distribution, and discharge coefficient. The CFD results were compared with experimental data, showing excellent agreement with errors in discharge coefficient predictions of less than 1%. This validation demonstrates the accuracy of the CFD model in capturing the behavior of geothermal two-phase flow through an orifice plate. The findings also provide valuable insights into the flow dynamics and pressure drop across the orifice, which are essential for improving the design and operation of geothermal systems. The simulation setup and methodology described in this study serve as a reliable reference for future studies and applications involving two-phase flow in geothermal systems. This research enhances the understanding of geothermal fluid dynamics and contributes to optimizing the design and performance of geothermal power plants.

1 INTRODUCTION

An orifice plate is a type of differential pressure flowmeter where the pressure drop occurred due to the restriction of an orifice plate inside the pipe. The measured pressure drop will be used to calculate the flow rate of the fluid. The concept of the conversion from pressure-drop to the flow rate is coming from Bernoulli's theorem (Reader-Harris, 2015). Many geothermal industries are using the orifice plate technique to measure a mass flow rate due to its simplicity, low installation cost, and reliability (Helbig & Zarrouk, 2012). The orifice plate technique can be applied to measure single and two-phase flow rate of geothermal fluid. Currently, five correlation equations can be used to calculate two-phase flow rate which has been developed by Murdock (1962), James (1965), Lin (1982), Zhang, Lu, and Yu (1992) and Helbig and Zarrouk (2012).

Computational fluid dynamics (CFD) is the use of computer numerical modeling to derive fluid flow behavior (Versteeg & Malalasekera, 1995). CFD is used to make a prediction of fluid flow in a certain system at a specified condition. Fluid flow prediction by CFD may be done with less cost and faster time than the experimental methods. The results of CFD fluid flows are also more comprehensive than many experimental methods which are limited by the availability, precision and accuracy of measuring instruments. In general, there are three steps in CFD numerical modeling; a pre-processor, solver and post-processor (Versteeg & Malalasekera, 1995). Each of the steps will contribute to the quality of the simulation results, thus the parameters must be considered carefully in every step to minimize error.

Some studies in geothermal applications have been done using CFD simulation; there are failure analysis (Fadli, Karim, Harahap, & Taufik, 2015; Mazur, Garcia-Illescas, & Porcayo-Calderon, 2009), two-phase flow in a separator vessel (Pointon, Mills, Seil, & Zhang, 2009; Purnanto, Zarrouk, & Cater, 2012; Zarrouk & Purnanto, 2014), wellbore or pipeline flow (Deendarlianto et al., 2016; Osato, Sato, & Kasai, 2016) and orifice plate flow (Hollingshead, 2011; Jithish & Kumar, 2015; Roul & Dash, 2012; Shah, Joshi, Kalsi, Prasad, & Shukla, 2012; Siba, Mahmood, Nuawi, Rasani, & Nassir, 2015; Urner, 1997; Zahariea, 2016).

In this work CFD was used to develop a three-dimensional model of geothermal two-phase fluid flow through an orifice plate. The aim of the study was to predict the downstream pressure of sharp-edge orifice plate in a two-phase pipeline. A predicted downstream pressure from CFD simulation was validated with pressure gauge monitoring data. The validated CFD model was used to predict the discharge coefficient ($C_{L/G}$ of the sharp-edge orifice plate, as well as the pressure and velocity distribution within the pipeline.

2 RELEVANT PREVIOUS WORKS

Several relevant CFD numerical studies are detailed here. Unfortunately, none of the studies present a CFD numerical simulation for geothermal two-phase flow through an orifice plate. However, the related information of computational setup will be useful for developing of geothermal two-phase flow CFD modeling. The summary of relevant previous studies is tabulated in Table 1.

Table 1. A comparison of numerical modeling setup from previous works.

Author	Geometry	Size (mm)	Working fluid	Model	Remarks
Pointon et al. (2009)	3-D geothermal cyclone separator (integrated water drum)	Vessel diameter: 3300	Two-phase fluid (geothermal)	RNG k-ε turbulence model	The combine CFD and FEA analysis were used to increase the performance of separator
Roul and Dash (2012)	2-D orifice plate inside the pipe	Pipe diameter: 40-60 β ratio: 0.54-0.73	Single-phase and two-phase fluids (water and air)	Realizable k-ε turbulence Eulerian-Eulerian models	The CFD models for thin and thick orifice plate has been developed to observes pressure drop, void fraction and slip ratio
Shah et al. (2012)	3-D orifice plate inside the pipe	Pipe diameter: 12.3-50.8 β ratio: 0.081-0.5	Single phase of water and air	Standard k-ε turbulence model	The standard k-ε model was success to represent a real fluid flow behavior through an orifice plate
Zarrouk and Purnanto (2014)	3-D geothermal cyclone separator	Vessel diameters: 2172, 2389 and 2134	Two-phase fluid (geothermal)	RNG k-ε turbulence mixture model	The CFD models were developed for three different inlet nozzle and correlated to the separation performance
Jithish and Kumar (2015)	3-D orifice plate inside the pipe	Pipe diameter: 25 β ratio: 0.44	Single phase of water	Standard k-ε turbulence model	The CFD model was used for predicting a discharge coefficient and turbulence effect
Siba et al. (2015)	3-D orifice plate inside the pipe	Pipe diameter: 10 β ratio: 0.2-0.5	Single phase of water and air	LRN k-ε turbulence model	The velocity profile and differential pressure have been investigated by CFD model for various Reynolds number and β ratio
Deendarlianto et al. (2016)	3-D pipe	Pipe diameter: 26	Two-phase fluid (water and air)	SST k-ω turbulence Vo model	The study of slug and plug flow regime using CFD numerical modeling
Zahariea (2016)	3-D orifice plate inside the pipe	Pipe diameter: 100 β ratio: 0.5	Single phase of water	SST k-ω turbulence model	A comparison of CFD models between concentric and eccentric orifice plate type

Pointon et al. (2009) and Zarrouk and Purnanto (2014) have studied the three dimensional CFD modeling of geothermal two-phase flow inside the cyclone separator by using RNG k-ε turbulence model. The model was used to evaluate the performance of separation system and provide the future recommendations. The performance of the separator must consider the key parameters including two-phase inlet geometry, vertical rise velocity, vessel proportions, steam outlet tube size and brine outlet nozzle size. The discrete phase model (DPM) was used to figure out the efficiency of separation process inside the cyclone separator based on particle trajectory with a two-way momentum coupling.

Roul and Dash (2012) have observed the two-phase and single-phase flow of air-water fluids through thin and thick orifice plate by two dimensional CFD modeling. The Eulerian multiphase model and the realizable k-ε turbulence have been used in the study. The residual continuity was achieved below 10^{-3}, while other variables were well convergence below 10^{-6}. The authors stated that the convergence criteria were enough to represent the real condition if there was no changing value of velocity and pressures at 5D upstream and 5D downstream from the orifice plate surface. The result of the model was used to correlate the pressure drop, void fraction and slip ratio of the fluids (single and two-phase) with the thickness of the orifice plate.

Shah et al. (2012) have presented a good match between the three-dimensional CFD models and the experimental data for single phase of water and air. The turbulence energy dissipation rate and discharge coefficient were used to validate the simulation result. All the solutions achieved convergence criteria with the number residual continuity was below 10^{-5}. In this study, some parameters were choosing in the numerical procedures to satisfy the result; standard k-ε turbulence model, semi-implicit pressure linked equation (SIMPLE) algorithm and second-order upwind of discretization. Furthermore, the parameters of under-relaxation were defined to 0.3 for the pressure, 0.7 for the momentum and 1 both for the density and body forces equations.

Jithish and Kumar (2015) have concentrated their study in discharge coefficient prediction and turbulence effect of water through an orifice plate by three dimensional CFD model. The experiment was used a 25 mm pipe diameter with 0.44 of β ratio. They concluded that CFD modeling was a powerful technique to determine the empirical orifice discharge coefficient.

Siba et al. (2015) have focused on the effect of Reynolds numbers and β ratio of the single fluid water and air to the orifice flow behavior. The Reynolds number and β ratio are varies between 5000 to 15000 and 0.2 until 0.5. The CFD model result was investigated to the velocity profile, the differential pressure and the mechanical properties. The simulation was fully converged with the final relative error was below 10^{-4}.

The CFD model of horizontal plug flow in two-phase 25 mm diameter pipe were studied by Deendarlianto et al. (2016) in order to carried out the phenomena of the flow. In this study, the mixture water and air were flowing through a pipe without an orifice plate. The volume of fluid (of) approach and the SST k-ω turbulence were used to the three-dimensional two-phase flow case. The unique things of this experiment were comparing the water volume fraction from visual observation with numerical result, and it resulted a good match.

A CFD modeling comparison of water flow through an eccentric and a concentric orifice plate was studied by Zahariea (2016). The author observed that the separated flow in upstream and downstream of the concentric orifice plate was contributed to the solid sedimentation at the bottom part of the pipe. While in the eccentric orifice plate type a solid sedimentation had not occurred because the orifice borehole was located at the bottom part of the pipe and prevented the separated flow at upstream and downstream part of the orifice plate.

Most of the previous work has been concentrated in orifice and pipe CFD flow modeling of non-geothermal fluids. There have been a few attempts to simulate geothermal fluids flow CFD numerical modeling. In this case, the previous works that used geothermal fluids in their CFD modeling are Pointon et al. (2009) and Zarrouk and Purnanto (2014). However, both studies were only discussed the geothermal fluid behavior inside the cyclone separator. This research work deals with the simulations of three-dimensional model of two-phase geothermal fluids through a concentric orifice plate. The field-testing data form geothermal wells are used to validate the CFD simulation result.

3 GOVERNING EQUATIONS

In general, the equations for measuring one-phase (1) and two-phase mass flow rate (2) can be stated as (Helbig & Zarrouk, 2012):

$$\dot{m}_{1\Phi} = \frac{F_a Y_G C_G A_{OP}}{\sqrt{1-\beta^4}} \sqrt{2\Delta p_{1\Phi} \rho}, \tag{1}$$

$$\dot{m}_{2\Phi} = K \frac{F_a Y_G C_G A_{OP}}{\sqrt{1-\beta^4}} \sqrt{2\Delta p_{2\Phi} \rho}, \tag{2}$$

where $\dot{m}_{1\Phi}$ [kg/s] is the mass flow rate of the single phase fluid, F_a is the orifice thermal expansion factor, Y_G is the liquid compressibility coefficient, C_G is the steam orifice discharge coefficient, A_{OP} [m^2] is orifice plate flow area, β is the ratio of the orifice diameter to the inside pipe diameter, $\Delta p_{1\Phi}$[bara] is measured differential pressure of the single phase fluid, ρ [kg/m^3] is the fluid density, $\dot{m}_{2\Phi}$ [kg/s] is the mass flow rate of the two-phase fluid, K is the two-phase coefficient, $\Delta p_{2\Phi}$[bara] is measured differential pressure of the two-phase fluid. The

most accurate and wider fluids enthalpy range of the geothermal two-phase orifice plate correlation was developed by Helbig and Zarrouk (2012):

$$\dot{m}_{2\Phi} = \left[\left(\frac{p_1}{11.5\times10^5}\right)^{D\sqrt{\frac{10^{-5}\Delta p_{2\Phi}}{D}}}\right]\left[\frac{\left(\frac{F_a\pi d^2}{4}\right)}{\left(\sqrt{1-\beta^4}\right)}\sqrt{2\Delta p_{2\Phi}}\right]$$

$$\left[\frac{(1-0.9x-0.1x^2)\left(C_L\sqrt{\rho_L}-Y_G C_G\sqrt{\rho_G}\right)}{(1+15x)}+\left(Y_G C_G\sqrt{\rho_G}\right)\right], \quad (3)$$

where p_1 [bara] is the upstream pressure of the orifice plate, d [m] is the orifice diameter, x is the dryness fraction of the fluid, C_L is the liquid orifice discharge coefficient, ρ_L [kg/m^3] is the liquid density and ρ_G [kg/m^3] is the steam density.

In numerical modeling, a governing equation selection is important to produce a good accuracy of modeling. The compatibility of selected governing equations with the data available is important to be considered. Siba et al. (2015) explained that continuity (4) and momentum equation (5) are the basic governing equations for the fluid through an orifice plate in the pipe:

$$\frac{\partial\rho}{\partial t}+\frac{\partial}{\partial x_i}(\rho u_i)=0, \quad (4)$$

$$\frac{\partial\rho}{\partial t}(\rho u_i)+\frac{\partial}{\partial x_j}(\rho u_i u_j)=-\frac{\partial p}{\partial x_j}+\frac{\partial}{\partial x_j}\left[\mu_t\left(\frac{\partial u_i}{\partial x_j}+\frac{\partial u_j}{\partial x_i}-\frac{2}{3}\delta_{ij}\frac{\partial u_i}{\partial x_i}\right)\right]+\frac{\partial}{\partial x_j}\left(-\rho\overline{u_i'u_j'}\right), \quad (5)$$

The mixture model of liquid and steam was choosing in the simulation because the study involved two-phase flow of geothermal fluids. Thus, the continuity and momentum equation can be stated as new expression.

$$\frac{\partial}{\partial t}(\rho_m)+\nabla(\rho_m\vec{v}_m)=0, \quad (6)$$

where $\vec{v}_m$ is the mass-averaged velocity (7) and ρ_m is the mixture density (8):

$$\rho_m=\sum_{k=1}^{2}\alpha_k\rho_k, \quad (7)$$

$$\vec{v}_m=\frac{\sum_{k=1}^{2}\alpha_k\rho_k\vec{v}_k}{\rho_m}. \quad (8)$$

If equations (7) and (8) are substituted into (6), the mixture continuity equation becomes:

$$\frac{\partial}{\partial t}\left(\sum_{k=1}^{2}\alpha_k\rho_k\right)+\nabla\left(\sum_{k=1}^{2}\alpha_k\rho_k\vec{v}_k\right)=0. \quad (9)$$

Considering to the mixture model, the momentum equation (10) is expressed as:

$$\frac{\partial}{\partial t}(\rho_m\vec{v}_m)+\nabla(\rho_m\vec{v}_m\vec{v}_m)=-\nabla p+\nabla\left[\mu_m\left(\nabla\vec{v}_m+\nabla\vec{v}_m{}^T_m\right)\right]+\rho_m\vec{g}+\vec{F}+\nabla\left(\sum_{k=1}^{2}\alpha_k\rho_k\,\vec{v}_{dr,k}\vec{v}_{dr,k}\right), \quad (10)$$

where $\vec{F}$ is a body force, μ_m is the mixture viscosity (11) and $\vec{v}_{dr,k}$ is the drift for secondary phase k (12):

$$\mu_m=\sum_{k=1}^{2}\alpha_k\mu_k, \quad (11)$$

$$\vec{v}_{dr,k}=\vec{v}_k-\vec{v}_m. \quad (12)$$

The final momentum equation for two-phase flow model resulted by substitution of equations (11) and (12) into equation (10):

$$\frac{\partial}{\partial t}(\rho_m\vec{v}_m)+\nabla(\rho_m\vec{v}_m\vec{v}_m)=-\nabla p+\nabla\left[\sum_{k=1}^{2}\alpha_k\mu_k\left(\nabla\vec{v}_m+\nabla\vec{v}_m{}^T_m\right)\right]$$

$$+\rho_m \vec{g} + \vec{F} + \nabla\left(\sum_{k=1}^{2} \alpha_k \rho_k (\vec{v}_k - \vec{v}_m)^2\right). \quad (13)$$

For three dimensional mixture flow, there is an additional volume fraction equation should be considered for the secondary phase p in the model (Deendarlianto et al., 2016).

$$\frac{\partial}{\partial t}(\alpha_p \rho_p) + \nabla(\alpha_p \rho_p \vec{v}_m) = -\nabla(\alpha_p \rho_p \vec{v}_{dr,p}) + \sum_{q=1}^{2}(\dot{m}_{qp} - \dot{m}_{pq}). \quad (14)$$

The flow of geothermal two-phase fluids through an orifice plate is turbulence with a Reynolds number larger than 5000 (Reader-Harris, 2015). To accommodate the turbulence flow, the governing equations for turbulence model must be considered. This turbulence viscosity model is referring to the Reynolds Average Navier Stokes (RANS) equations. There are some of turbulence models available in ANSYS (ANSYS, 2013). However, not all the models must be used in the simulation. The selection of an appropriate turbulence model may different for each study cases. Jithish and Kumar (2015) stated that $k-\varepsilon$ turbulence models are the most frequently and widely used in industrial applications and requires less computational effort compared to other turbulence models. In this study, the realizable $k-\varepsilon$ and shear-stress transport (SST) $k-\omega$ were used to simulate the geothermal two-phase fluid through an orifice plate.

The transport equations for k (15) and ε (16) in realizable $k-\varepsilon$ turbulence model is:

$$\frac{\partial}{\partial t}(\rho k) + \frac{\partial}{\partial x_j}(\rho k u_j) = \frac{\partial}{\partial x_j}\left[\left(\mu + \frac{\mu_t}{\sigma_k}\right)\frac{\partial k}{\partial x_j}\right] + G_k + G_b - \rho\varepsilon - Y_M + S_k, \quad (15)$$

$$\frac{\partial}{\partial t}(\rho \varepsilon) + \frac{\partial}{\partial x_j}(\rho \varepsilon u_j) = \frac{\partial}{\partial x_j}\left[\left(\mu + \frac{\mu_t}{\sigma_\varepsilon}\right)\frac{\partial \varepsilon}{\partial x_j}\right] + \rho C_1 S_\varepsilon - \rho C_2 \frac{\varepsilon^2}{k + \sqrt{v\varepsilon}} + C_{1\varepsilon}\frac{\varepsilon}{k} C_{3\varepsilon} G_b + S_\varepsilon, \quad (16)$$

where the constants of $C_{1\varepsilon} = 1.44$, $C_2 = 1.9$, $\sigma_k = 1.0$ and $\sigma_\varepsilon = 1.2$. While C_1 can be expressed as:

$$C_1 = max\left[0.43, \frac{\frac{k\sqrt{2S_{ij}S_{ij}}}{\varepsilon}}{\frac{k\sqrt{2S_{ij}S_{ij}}}{\varepsilon} + 5}\right]. \quad (17)$$

The final equation for k (18) and ε (19) becomes:

$$\frac{\partial}{\partial t}(\rho k) + \frac{\partial}{\partial x_j}(\rho k u_j) = \frac{\partial}{\partial x_j}\left[(\mu + \mu_t)\frac{\partial k}{\partial x_j}\right] + G_k + G_b - \rho\varepsilon - Y_M + S_k, \quad (18)$$

$$\frac{\partial}{\partial t}(\rho \varepsilon) + \frac{\partial}{\partial x_j}(\rho \varepsilon u_j) = \frac{\partial}{\partial x_j}\left[\left(\mu + \frac{\mu_t}{1.2}\right)\frac{\partial \varepsilon}{\partial x_j}\right] + \rho S_\varepsilon max\left[0.43, \frac{\frac{k\sqrt{2S_{ij}S_{ij}}}{\varepsilon}}{\frac{k\sqrt{2S_{ij}S_{ij}}}{\varepsilon} + 5}\right]$$

$$-1.9\rho\frac{\varepsilon^2}{k + \sqrt{v\varepsilon}} + 1.44\frac{\varepsilon}{k} C_{3\varepsilon} G_b + S_\varepsilon. \quad (19)$$

The transport equations of k (20) and ω (21) in SST $k-\omega$ turbulence model are stated as:

$$\frac{\partial}{\partial t}(\rho k) + \frac{\partial}{\partial x_i}(\rho k u_i) = \frac{\partial}{\partial x_j}\left[\Gamma_k \frac{\partial k}{\partial x_j}\right] + G_k - Y_k + S_k, \quad (20)$$

$$\frac{\partial}{\partial t}(\rho \omega) + \frac{\partial}{\partial x_i}(\rho \omega u_i) = \frac{\partial}{\partial x_j}\left[\Gamma_\omega \frac{\partial \omega}{\partial x_j}\right] + G_\omega - Y_\omega + D_\omega + S_\omega, \quad (21)$$

where the effective diffusivities equations are:

$$\Gamma_k = \mu + \frac{\mu_t}{\sigma_k}, \quad (22)$$

$$\Gamma_\omega = \mu + \frac{\mu_t}{\sigma_\omega}. \quad (23)$$

Considering to the effective diffusivity's equations (22) and (23), the final expressions of k (24) and ω (25) are:

$$\frac{\partial}{\partial t}(\rho k) + \frac{\partial}{\partial x_i}(\rho k u_i) = \frac{\partial}{\partial x_j}\left[\left(\mu + \frac{\mu_t}{\sigma_k}\right)\frac{\partial k}{\partial x_j}\right] + G_k - Y_k + S_k, \quad (24)$$

$$\frac{\partial}{\partial t}(\rho\omega) + \frac{\partial}{\partial x_i}(\rho\omega u_i) = \frac{\partial}{\partial x_j}\left[\left(\mu + \frac{\mu_t}{\sigma_\omega}\right)\frac{\partial \omega}{\partial x_j}\right] + G_\omega - Y_\omega + D_\omega + S_\omega. \quad (25)$$

4 METHODOLOGY

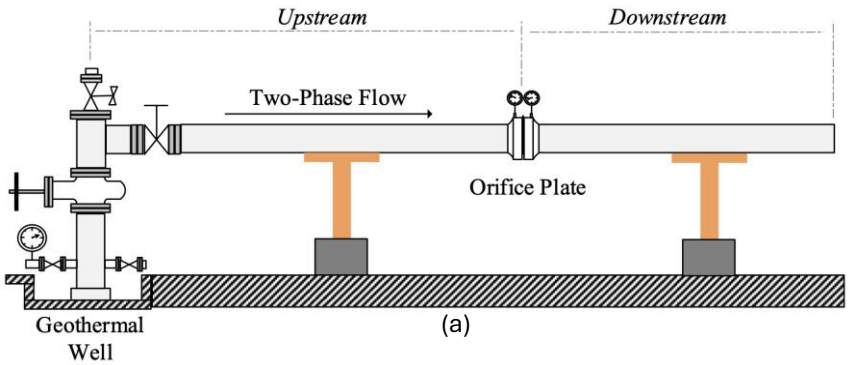
The parameter inputs for CFD simulation were taken from the field experimental data of geothermal well UBL-A, Ulu Belu, Indonesia. These field experimental data including geometry, upstream pressure, differential pressure, dryness, fluid density, fluid viscosity and mass flow rate (Table 2).

Table 2. Data parameters from the field experiment of geothermal well UBL-A.

Parameters	Unit	Value
	Geometry	
D	mm	431.80
d	mm	316.00
$\beta\ (d/D)$		0.73
e	mm	3.24
E	mm	9.18
Tapping type		Flange
Orifice plate type		Sharp-edge concentric
	Operating conditions	
Fluid		Steam-Brine (Mixture)
p_1	bara	12.95
	Pa	1,295,000
p_2	bara	12.73
	Pa	1,273,176
Δp	bara	0.22
ρ_G	kg/m^3	6.59
ρ_L	kg/m^3	874.48
μ_G	kg/mgs	0.0000155
μ_L	kg/mgs	0.0001399
h	kJ/kg	1,095
$\dot{m}$	kg/s	124
x	%	14.24
$\dot{m}_G$	kg/s	17.67
$\dot{m}_L$	kg/s	106.44

4.1 Flow Domain

The three-dimensional model was built using CAD design modeler that integrated with ANSYS version 17. The horizontal of geothermal two-phase fluid flow through a sharp-edge orifice plate in a pipe and the hook instrumentation hook up are shown in Fig. 1 (a) and Fig. (b), while the solid domain geometry is presented in Fig. 1 (c). The two-phase flow model was a segmental pipeline 6000 mm length with 432 mm internal pipe diameter and 316 mm concentric orifice diameter which is located at the center of the pipe. Furthermore, the thickness of the plate (E) is 9.2 mm and the sharp-edge thickness (e) is 3.2 mm with 45^o of bevel angle. The major axis of the pipe length was aligned with the x-axis of the domain, the minor axis in y and z was the vertical direction.



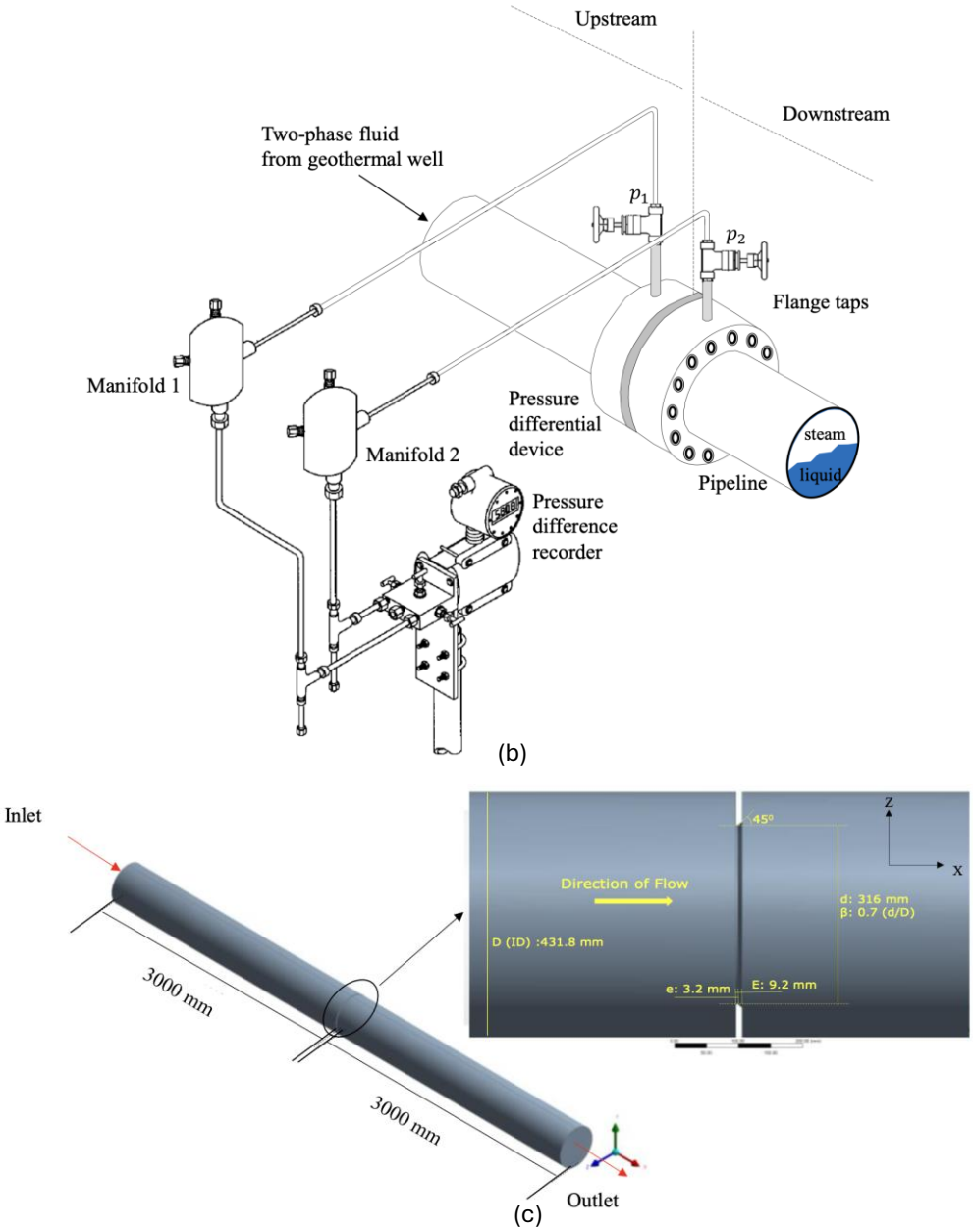


Figure 1. Geometric arrangement, showing (a) typical orifice flowmeter position at geothermal well facilities, (b) pressure differential flow meter tapings with instrumentation connections and (c) three dimensional of sharp-edge concentric orifice plate flow model for the CFD simulation.

4.2 Mesh Generation

An appropriate mesh for the flow solver simulation was developed by using mesh application from ANSYS (version 17) workbench as shown in Fig. 2. Unstructured triangular fluid domain meshes have been created for the simulations with the minimum edge length of the triangles was 3.2 mm. The meshes quality was observed with skewness and aspect ratio to ensure that the result of solution is representing the correct model of two-phase fluid flow movement through an orifice plate. An average value of skewness and aspect ratio were 0.23 and 4.82. While Typical mesh of 432 mm intenal pipe diameter including the concentric sharp-edge orifice is shown in Fig. 2. A smooth transition of inflation was generated to increase nodes number near surface with a transition ratio of 0.272, a maximum of 5 layers and a growth rate of 1.2. All following simulations have used 2,156,968 elements and 831,859 nodes of the meshes.

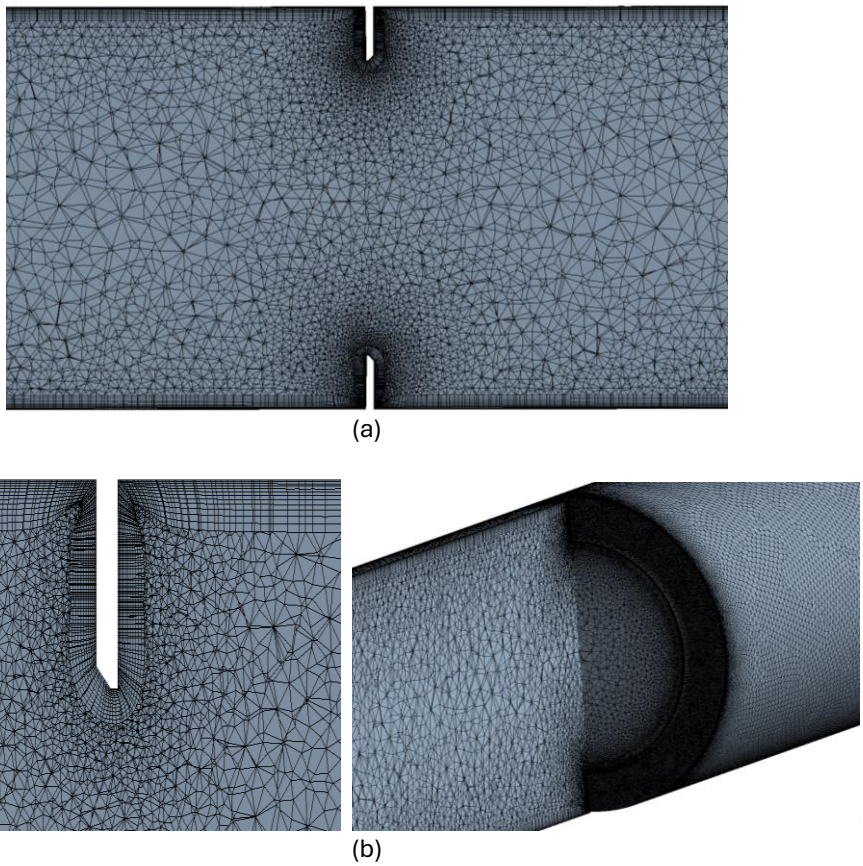


Figure 2. Mesh generation: (a) symmetry plane detail and (b) concentric sharp-edge orifice and section plane detail.

4.3 Initial and Boundary Conditions

The geothermal two-phase fluid domain was modeled using Fluent ANSYS version 17 with a reference pressure 12.95 bara (1,295 kPa) at upstream pressure of the flange tapping. The position of upstream pressure tapping was located at -0.0254 m from the surface of orifice plate in the x direction. Gravitational acceleration was set to -9.81 m/s^2 in y direction. The general settings were choosing to solve the Reynolds-Averaged Navier-Stokes (RANS) equations in the initial and boundary conditions setup: steady pressure-based solver; mixture model; realizable k-ε and SST k-ω turbulence viscous model. In the multiphase mixture model, water-vapor was selected as primary phase (phase 1) and water-liquid as secondary phase (phase 2). A reference density and dynamic viscosity for phase 1 were 6.59 kg/m^3 and 1.55×10^{-5} kg/mgs, while for phase 2 were 874.48 kg/m^3 and 13.99×10^{-5} kg/m.s. To carry out the simulations, the inlet zone was set to mass flow condition with 17.67 kg/s of the phase 1 and 106.44 kg/s for the phase 2. In other domain boundaries, pressure was set at the outlet and no-slip condition at wall zone was implemented.

4.4 Solution Parameters

A coupled of pressure-velocity coupling scheme in the solution method was used to solve the flow domain because this algorithm has a superior performance compared to other schemes and appropriate with steady-state flow and pressure-based solver (ANSYS, 2013). For the steady state coupled solver with complex three dimensional cases, the default Courant number (Co) 200 need to be decreased between 20-50 to achieve more numerical efficiency (ANSYS, 2013). In this study, the Courant number was set to 35. The timestep duration was set to 0.001 s because this value was found to be adequate to authorize geothermal two-phase flow models to develop successfully, the number was same with the two-phase flow CFD modeling from Deendarlianto et al. (2016). In spatial discretization solution, least squares cell based, and body force upwind had used in gradient and pressure. The first-order upwind accuracy scheme was chosen for momentum, volume fraction, turbulence kinetic energy and dissipation rate. All the solutions will converge when the residual continuity, x-y-z velocity, turbulence kinetic energy, dissipation rate (for realizable k-ε model) and specific of dissipation rate (for SST k-ω model) achieved a value 10^{-5}. An initial value of the solution may help the solution to achieve the convergence criteria (Purnanto et al., 2012). In this work, standard initialization was used with 27 m/s an initial x-axis velocity.

A summary of the parameters setup that used in all the three-dimensional CFD simulations is shown in Table 3.

Table 3. A summary of CFD modeling parameters setup.

Parameters setup		Unit	Model	
			1	2
Meshing	Nodes		831,859	
	Elements		2,156,968	
	Average of skewness		0.2341	
	Average of aspect ratio		4.8168	
Setup				
General	Solver type		Pressure-Based	
	Solver time		Steady	
	Gravity	m/s^2	-9.81 at y-axis	
Models	Multiphase model		Mixture	
	Phase 1		Water-vapor	
	Phase 2		Water-liquid	
	Viscous model		Realizable k-ε	SST k-ω
Materials	ρ phase 1	kg/m^3	6.59	
	ρ phase 2	kg/m^3	874.47	
	μ phase 1	kg/m.s	$1.55x10^{-5}$	
	μ phase 1	kg/m.s	$13.99x10^{-5}$	
Boundary Conditions	Operating pressure	Pa	1,295,000 at -0.0254 m (x-axis)	
	Inlet type		mass-flow-inlet	
	Mass flow rate phase 1	kg/s	17.67	
	Mass flow rate phase 2	kg/s	106.44	
Solution				
Solution methods	Pressure-velocity coupling		Coupled	
	Spatial discretization			
	Gradient		Least squares cell based	
	Pressure-velocity coupling		Body force weight	
	Momentum		First order upwind	
	Volume fraction		First order upwind	
	Turbulence kinetic energy		First order upwind	
	Specific dissipation rate		First order upwind	
Solution controls	Volume fraction courant number (Co)		35	
Residual monitor (target)	Continuity		Below 10^{-4}	
	x, y, z velocity		Below 10^{-4}	
	k or ω		Below 10^{-4}	
Solution initialization	Initialization methods		Standard initialization	
	Initial values (x velocity)	m/s	27	
Run Calculation	Pseudo time step	s	0.001	

5 RESULTS

5.1 Flow Development Results

In initial numerical experiments, the realizable k-ε turbulence model was used to investigate the simulation parameters setup selection. For the next simulation, the SST k-ω turbulence viscous model was developed and used same parameters setup in the realizable k-ε turbulence model. The simulation for realizable k-ε turbulence model was fully converged after 783 iterations which indicated by the entire residuals fell to 10^{-5}, while the SST k-ω turbulence model needs a higher number of iterations (1500) to achieve convergence criteria.

5.2 Computed of Pressure and Velocity

Fig. 3 and Fig.4 shows the geothermal two-phase fluids pressure and velocity contours for realizable k-ε and SST k-ω turbulence viscous model in the x-y plane, while the velocity streamline for both models is displayed in Fig. 5.

Predicted pressure contours from CFD simulation in Fig. 3 illustrates the two-phase flow pressure changes from the inlet to the outlet direction. The pressure is significantly decreased near the upstream of the orifice plate and achieves the lowest point at the downstream of orifice which called as vena-contracta zone (blue color); however, this visual phenomenon is only clear for SST k-ω model. The pressure decline happened due to the flow restriction by the sharp-edge orifice plate which has lower diameter then inside pipe diameter (β=0.7).

The geothermal two-phase velocity is increased almost double after through an orifice plate, from 27 m/s at the inlet point to 53 m/s at 20 cm downstream side either realizable k-ε or SST k-ω turbulence model (Fig. 4). Additionally, the vena-contracta zone is visualized clearly in the velocity streamline (Fig. 5) and it is indicated by the circular stream on the top and bottom part of the pipe (blue color) with approximately length of the zone is 1.5 m at downstream side.

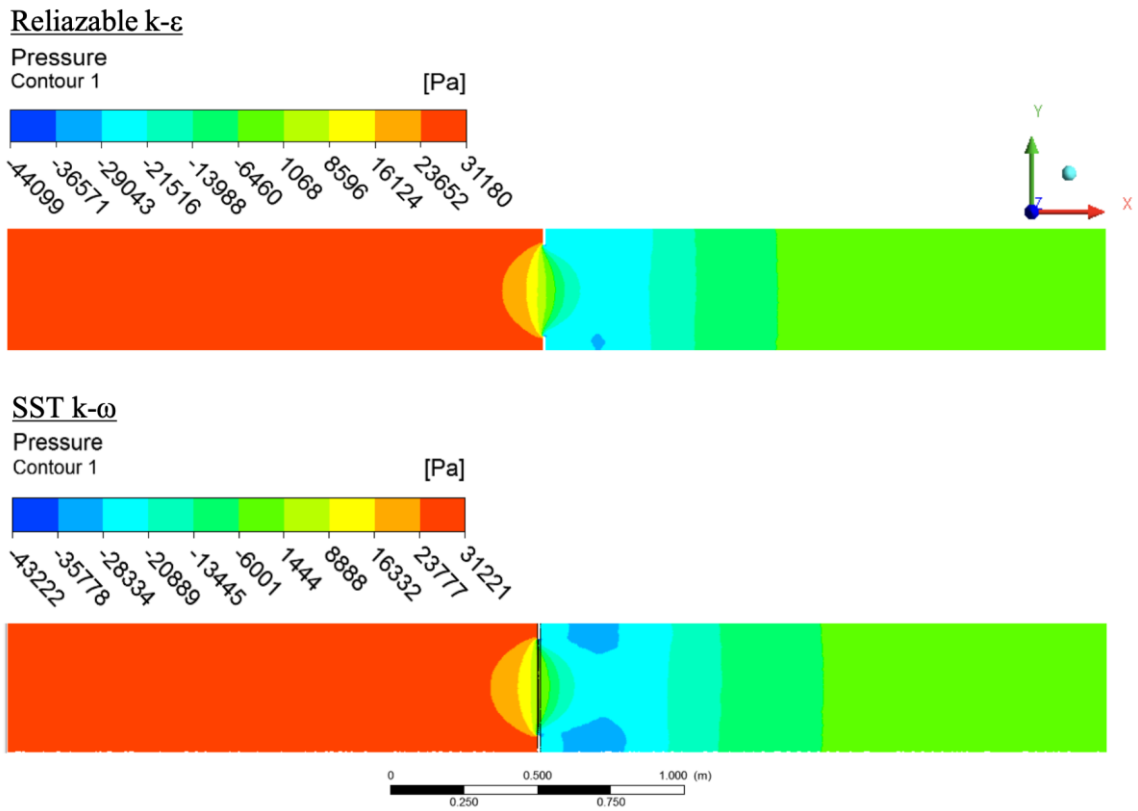


Figure 3. Pressure contour for realizable k-ε and SST k-ω turbulence viscous model at x-y plane.

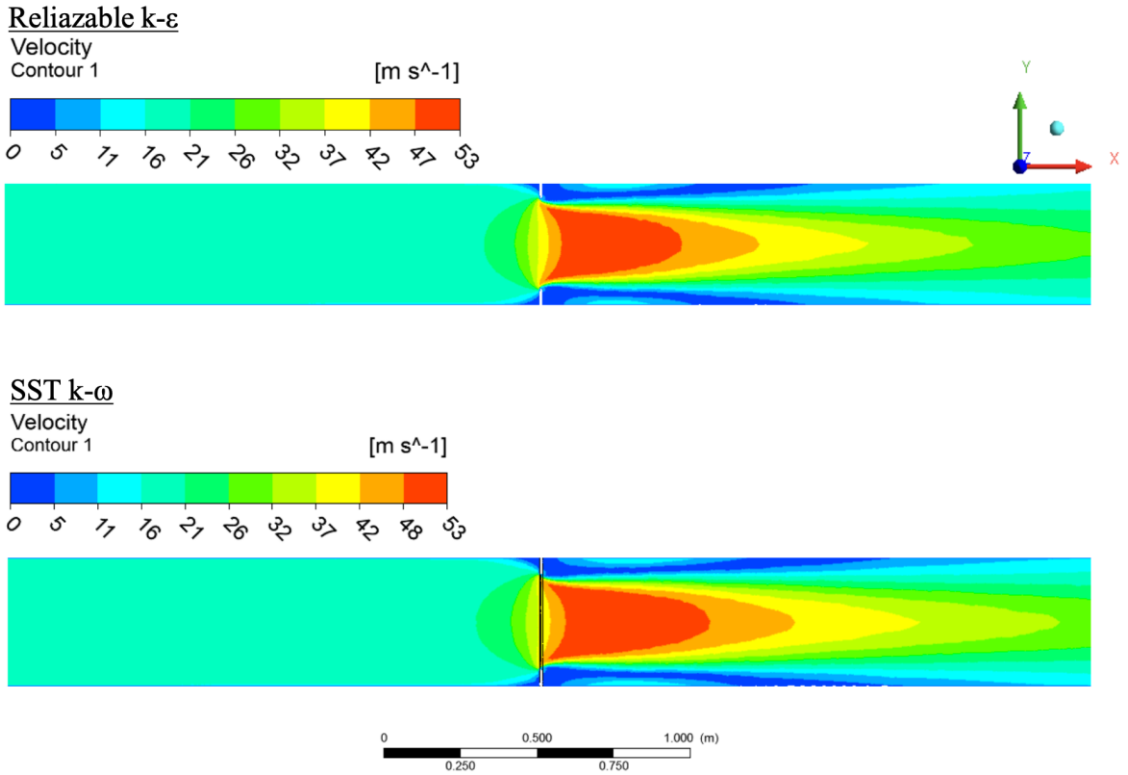


Figure 4. Velocity contour for realizable k-ε and SST k-ω turbulence viscous model at x-y plane.

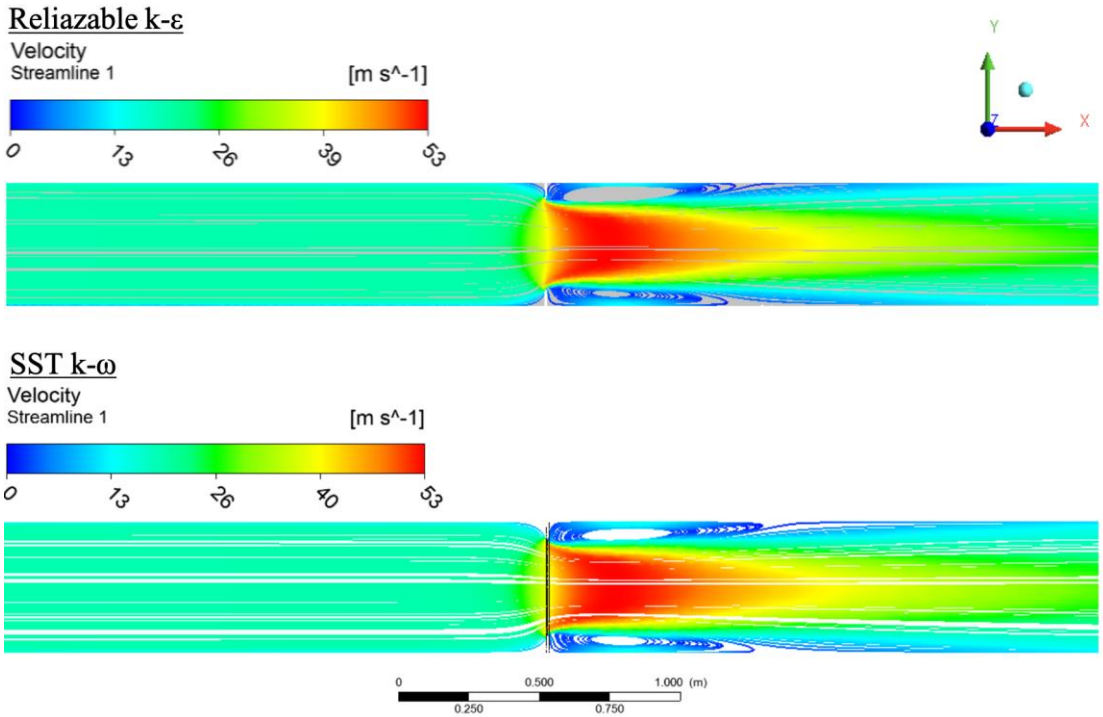


Figure 5. Velocity streamline for realizable k-ε and SST k-ω turbulence viscous model at x-y plane.

Radial velocity profile with various axial locations for realizable k-ε and SST k-ω turbulence is shown in Fig. 6. The gradual velocity is illustrated for nine different locations where the orifice plate is adjusted as starting point (x=0.00 m). The location points in the plots are x=-3.00 m (inlet), x=0.00 m (orifice), x=0.05 m, x=0.10 m, x=0.20 m, x=1.00, x= 2.00 m, x=2.50 m and x=3.00 m (outlet).

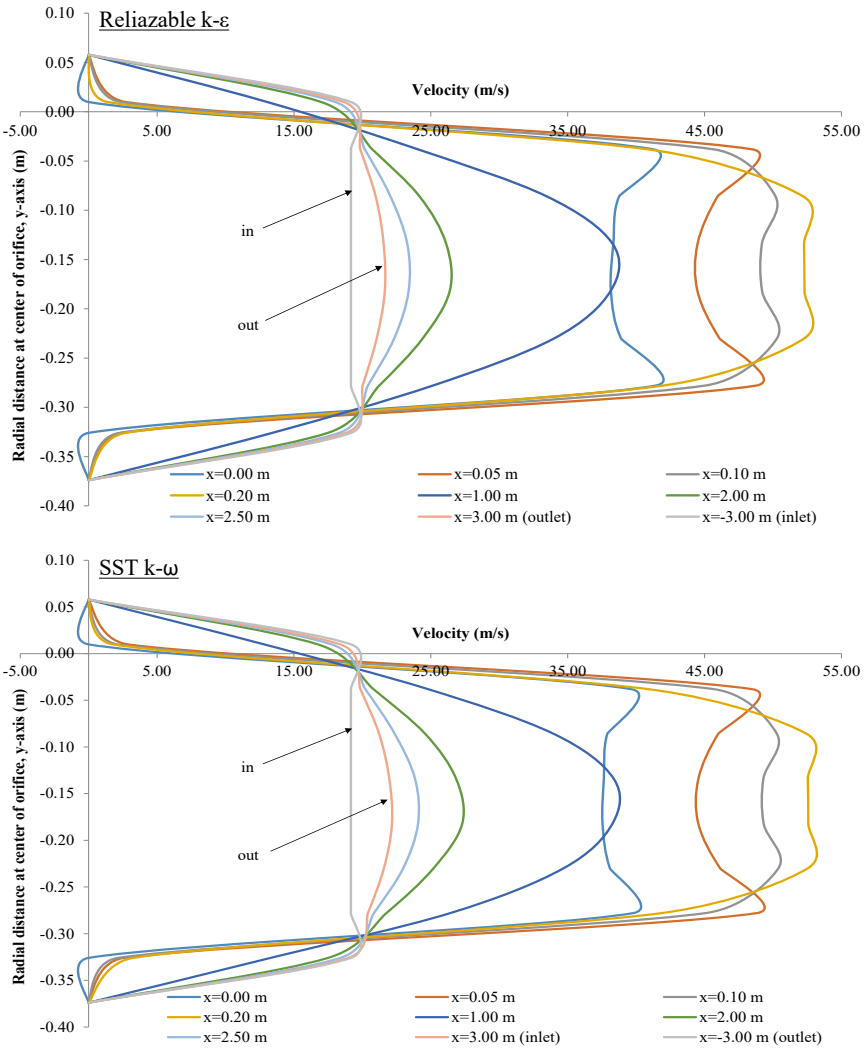


Figure 6. Computed radial velocity profile at various x-axis locations for the turbulence viscous model; (a) realizable k-ε and (b) SST k-ω turbulence

A comparison of computed turbulence kinetic energy (k) radial profile for two different turbulence models (realizable k-ε and SST k-ω) at the center of orifice as shown in Fig. 7.

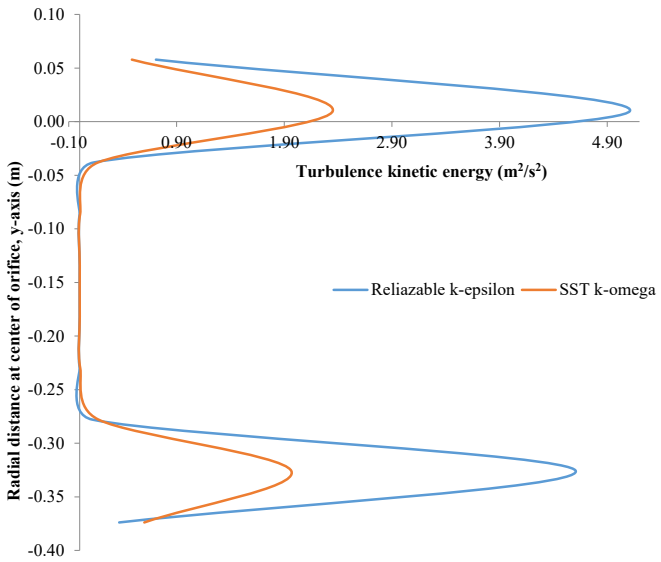


Figure 7. Computed radial profiles of turbulence kinetic energy (k) at the center of sharp-edge orifice plate for realizable k-ε and SST k-ω turbulence viscous model.

6 DISCUSSION

Some CFD modeling parameters setup has observed to achieve the residuals target (10^{-5}). The realizable k-ε model was implemented as an initial turbulence model and further work was done with SST k-ω. Based on the several trials, some parameter selections will contribute to produce a good and appropriate solution including mesh number, viscous turbulence model, pressure-velocity coupling method, spatial discretization, volume fraction courant number (Co) and pseudo time step as stated in Table 3. Both models were achieved the residuals target after 783 (realizable k-ε) and 1500 iteration steps (SST k-ω).

Based on the solution results, the SST k-ω model required greater computational effort than realizable k-ε to solve the simulation problems. However, the SST k-ω will produce more accurate and robust results for wider flow problems (ANSYS, 2013; Matsubara, Kuo, & Wu, 2013). The turbulence kinetic energy (k) of the models in Fig. 7 shows the same similar radial profile, the turbulence kinetic energy is increased near to the wall and achieve maximum value 5.11 m^2/s^2 for realizable k-ε and 2.35 m^2/s^2 for SST k-ω. This phenomenon is occurred due to the flow separation process (Shah et al., 2012).

The turbulence flow for both methods in several axial locations has investigated. As seen in Fig. 6, the turbulence flow at the outlet points (x=3.00 m) still not in fully developed which indicated by comparison of the velocity gradient at inlet point. The fully developed turbulence conditions will occur at some point after the outlet. The computational domain was limited to 3 m upstream and downstream of the orifice plate (Fig. 1).

The computed pressure profile of two-phase geothermal fluids across the concentric sharp-edge orifice plate (x-axis direction) from CFD simulation is shown in Fig. 8. For validating the model of geothermal two-phase fluids through an orifice plate, a comparison of calculated and measured pressure drop is necessary. In this work, a predicted pressure drop was calculated from the different value of upstream (p_1) and downstream pressure (p_2) in the pressure profile plot (Fig. 8), while a measured pressure drops (Δp) was obtained from experimental data.

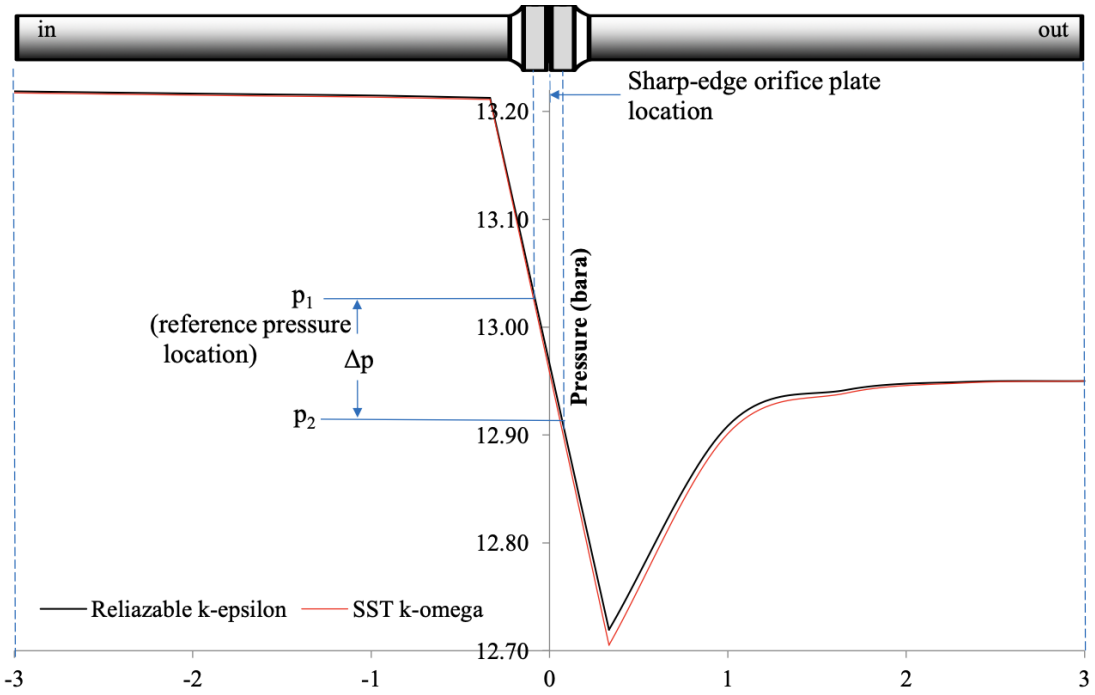


Figure 8. Predicted pressure profile of the geothermal two-phase flow through a sharp-edge orifice plate at the center of pipe with x-axis direction for realizable k-ε and SST k-ω turbulence viscous model.

The relative error of CFD pressure for realizable k-ε and SST k-ω are less than 83%. The relative error of SST k-ω is lower than realizable k-ε turbulence model. This means that the SST k-ω is more accurate to solve the three-dimensional model of geothermal two-phase flow through an orifice plate problem than realizable k-ε. The pressure drops from the experimental data and CFD models has been taken to calculate the fluids discharge coefficient (C) and mass flow rate. The liquid (C_L) discharge coefficient, steam discharge coefficient (C_G) and mass flow rate were calculated using Helbig and Zarrouk correlation (Helbig & Zarrouk, 2012). Table 4 gives a comparison of the experimental data and simulated value results. In general, both models are in good

agreement to predict the discharge coefficient. The relative error for discharge coefficient is less than 1%. It is noted that the SST k-ω is more accurate and can be used as a reference for further similar CFD model.

Table 4. Comparison of experimental data and the simulation result to validate the CFD models.

Case no.	Viscous turbulent model	Pressure drop, Δp (bar)		Discharge coefficient, C					
				Liquid, C_L			Steam, C_G		
		Measured	CFD	Experiment	CFD	Rel. error (%)	Experiment	CFD	Rel. error (%)
1	Realizable k-ε	0.21824	0.03758	0.59537	0.59634	0.1627	0.59561	0.59666	0.1762
2	SST k-ω		0.03855		0.59632	0.1600		0.59664	0.1733

6.1 Other Pressure Differential Flow Meter Results

6.1.1 Transient Model Analysis

A transient model was used to validate and refine the steady-state model due to the unavailability field experimental data for these flow meters (Mubarok et al., 2019; Denton, 2009). The transient model represents the natural variations in time and space of two-phase fluid flow phenomena (Deendarlianto et al., 2016; Dehkordi et al., 2017). The geometry of the Nozzle flow meter was selected for validating the steady-state model. The maximum Courant number (Cr) was set to 20, with 0.0005-second time steps, 150-time steps and 0.075 s total simulation time; iterative convergence was achieved for every time step. A comparison of the predicted net pressure drops for the Nozzle flow meter model is shown in Table 7. The predicted net pressure drop of the steady-state model with the second-order method for momentum (Model 3) is smaller than with the first-order method (Model 2) when compared with the transient model (Model 1).

Table 5. Net pressure drops of transient and steady state models.

Model	Time	Momentum of spatial discretization	Predicted Δp_{net} (Pa)	Relative error (%)
1	Transient	First-order	23,679	-
2	Steady-state	First-order	22,859	3.46
3	Steady-state	Second-order	23,408	1.14

To confirm the validity of the steady-state model, the velocity and turbulent kinetic energy were compared with the time average values, as shown in Fig. 9. From X=0 m to X=0.75 m, Model 1 and Model 3 are almost identical, especially for flow velocity between 90 to 120 m/s. The high-velocity region in Model 2 shows the fluids are in a plug flow condition. The kinetic energy field (Fig. 9b) shows similar behavior. Based on the predicted net pressure drop results and velocity distribution comparison, the steady-state model with second-order momentum term was chosen for all the other flow meters under study.

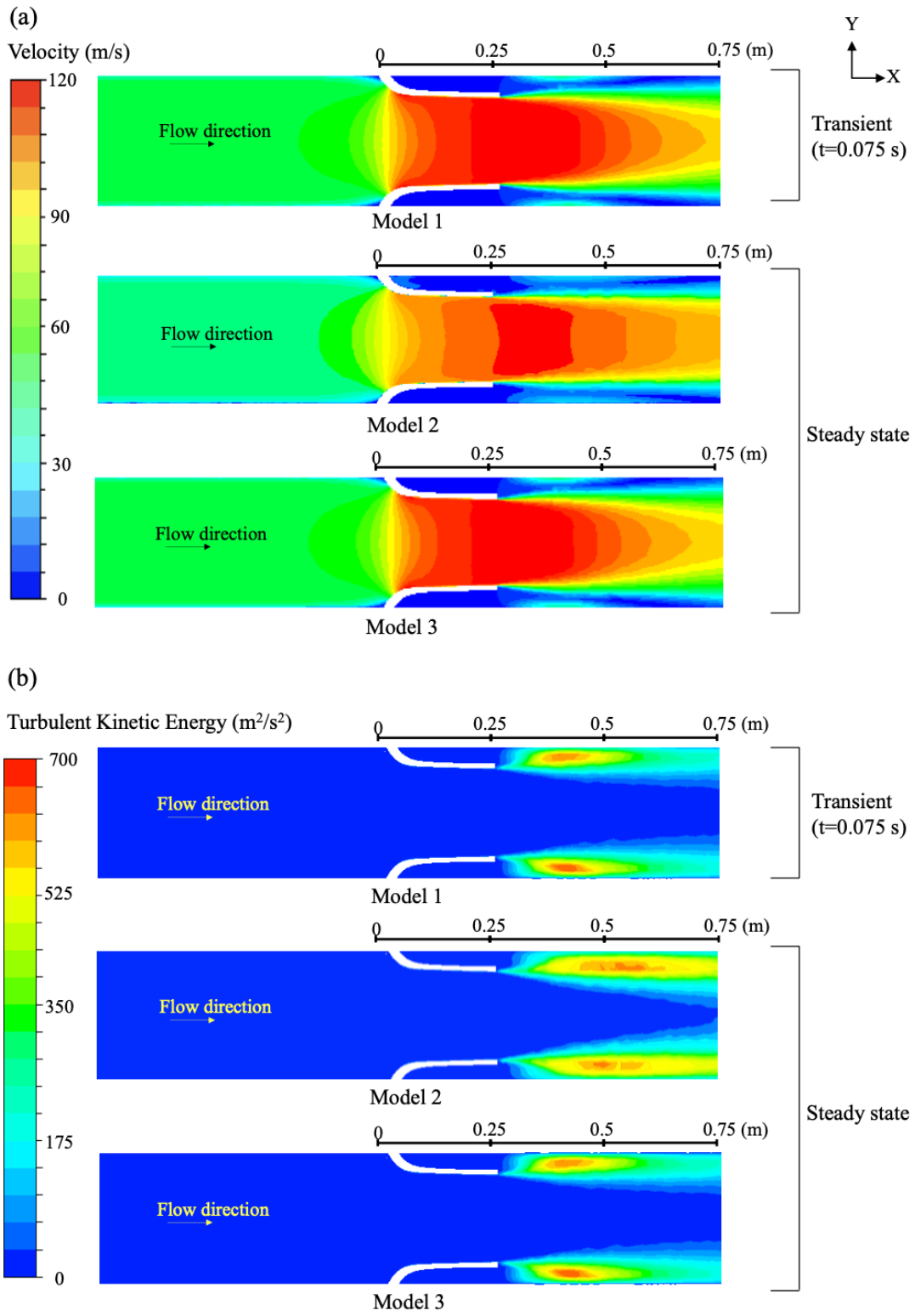


Figure 9. Steady-state and time-averaged transient Nozzle models in a vertical plane in terms of (a) velocity and (b) turbulent kinetic energy (Mubarok et al., 2019).

6.1.2 Pressure Distribution and Net Pressure Drop

Fig. 10 shows the pressure distribution in concentric orifice, top eccentric orifice, bottom eccentric orifice, segmental orifice, Nozzle and Venturi flow meters, respectively, along the entire two-phase fluid domain. No significant pressure change can be seen in the upstream region for all flow meters; in this region, the pressure drop is only affected by pipeline wall roughness.

The pressure reaches its lowest value (5.7×105 Pa) at X=0.1 m with the orifice flow meters (Figs. 10a–10d) before increasing beyond this point and becoming constant after 2.5 m downstream. When comparing the value of the inlet and outlet pressures, the net pressure drop of the segmental orifice (Fig. 10d) is lower than those of the concentric orifice (Fig. 10a), top eccentric orifice (Fig. 10b) and bottom eccentric orifice (Fig. 10c). However, the lowest net pressure drop is observed for the Venturi flow meter (Fig. 10f), followed by the Nozzle flow meter (Fig. 9e). The gradual restriction of the Nozzle and the Venturi's geometry provides lower resistance to the two-phase fluid flow and produces higher pressure recovery at the outlet (Fig. 9).

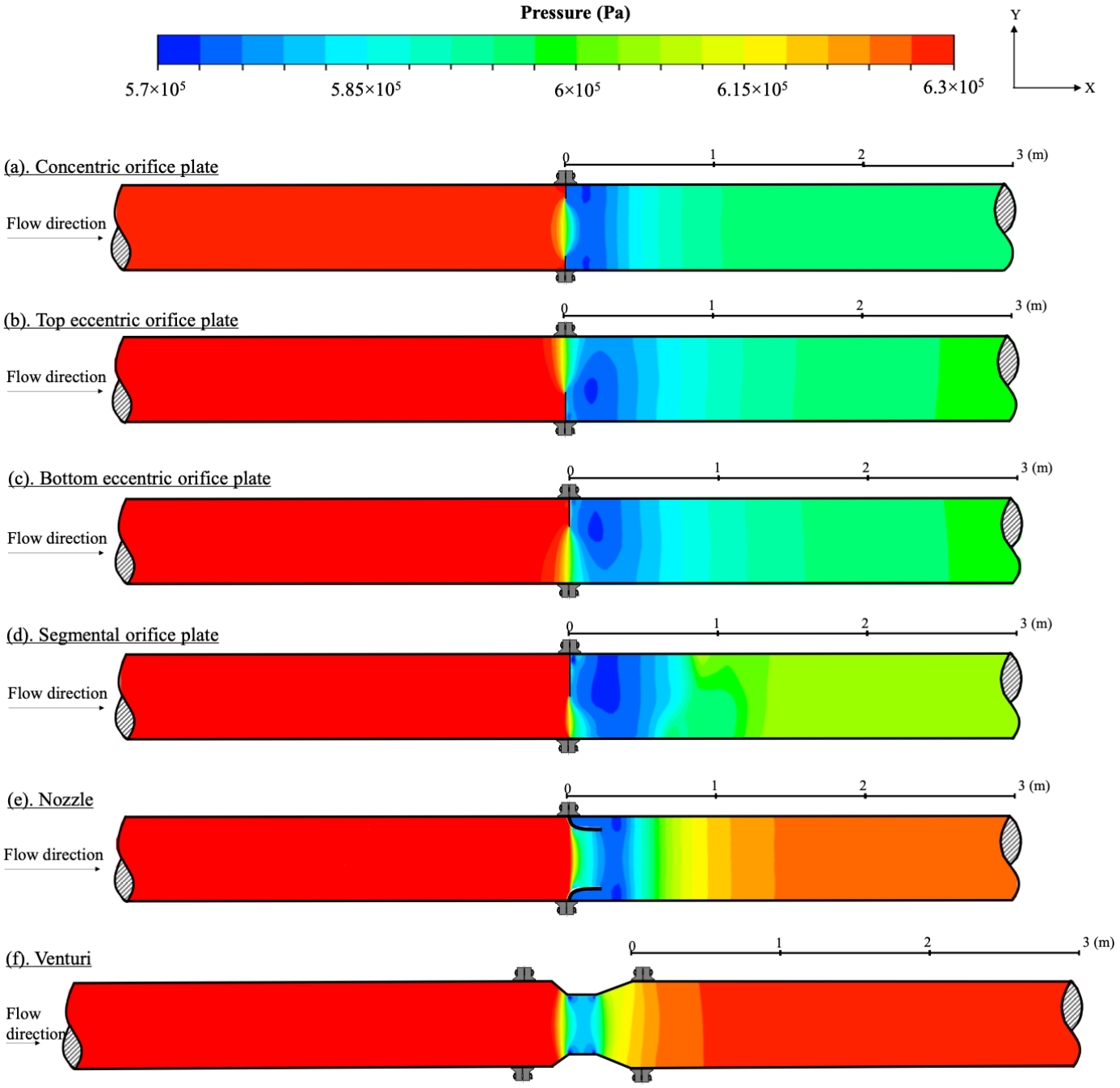


Figure 10. Pressure distribution for (a) concentric orifice, (b) top eccentric orifice, (c) bottom eccentric orifice, (d) segmental orifice, (e) Nozzle and (f) Venturi in vertical plane with inlet parameters $\dot{m}_g$=9.07 kg/s, $\dot{m}_f$=13.72 kg/s, h=1506.23 kJ/kg, x=39.82% (Mubarok et al., 2019)..

The net pressure drops and its correlation to the mass flow rate for the six types of flow meters is shown in Fig. 11. The Venturi flow meter has the lowest net pressure drop followed by the Nozzle and orifice flow meters. The conical convergent-divergent section and cylindrical throat of the Venturi flow meter maximize the pressure recovery for a two-phase fluid (Bai and Zheng, 2017; Steven and Hall, 2009).

Of the orifice flow meters, the segmental type had the lowest net pressure drop compared with the concentric and eccentric models. The segmental orifice has a circular segment at the bottom part of the pipe that enables the liquid phase to pass through the orifice plate more easily than other orifice plate types. When the orifice hole is positioned centrally, the net pressure drop is significantly higher (±15%). From Fig. 10, the net pressure drop for two-phase flow can be reduced by up to 6% by simply shifting the orifice opening location from the centre of the pipe to the top or bottom, creating an eccentric orifice plate (Mubarok et al., 2019).

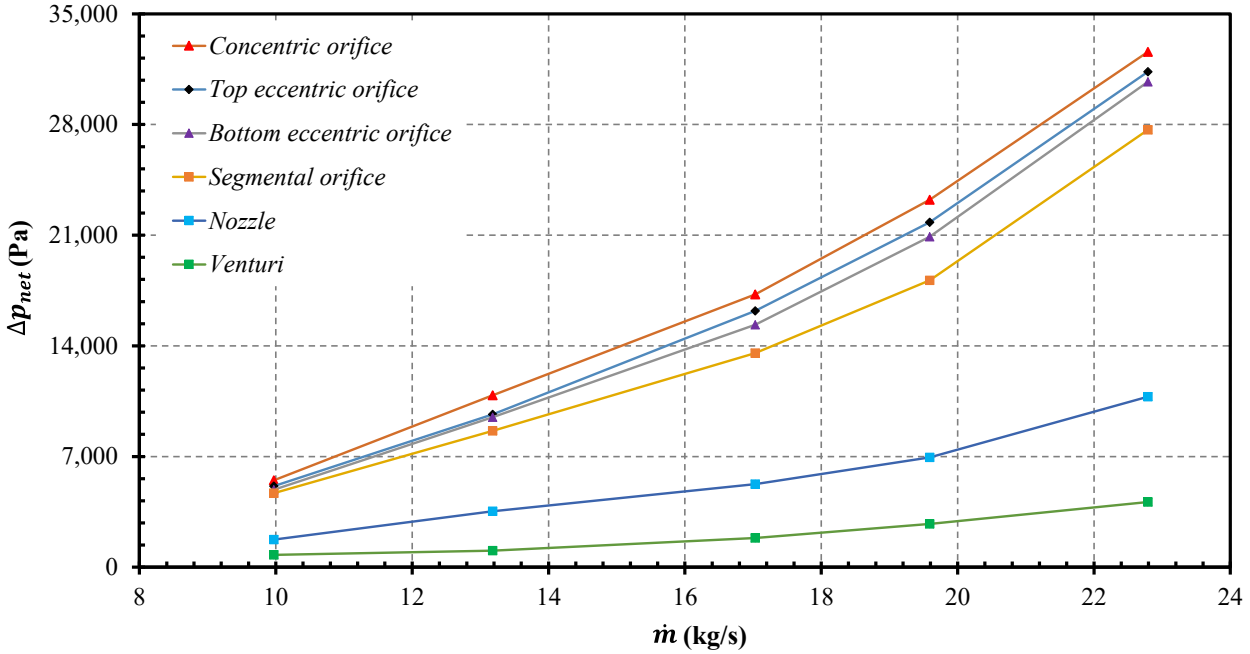


Figure 11. Net pressure drop of pressure differential flow meters with mass flow rate (Mubarok et al., 2019).

6.1.3 Two-phase Fluid Velocity

The velocity distribution for the concentric orifice, top eccentric orifice, bottom eccentric orifice, segmental orifice, Nozzle and Venturi flow meters in the vertical plane is shown in Fig. 12. The velocity can be seen to increase through the flow meters with a maximum value (120 m/s) downstream close to the flow meter restriction. A vena contracta zone (Shan et al., 2016) is formed with a different shape for each flow meter.

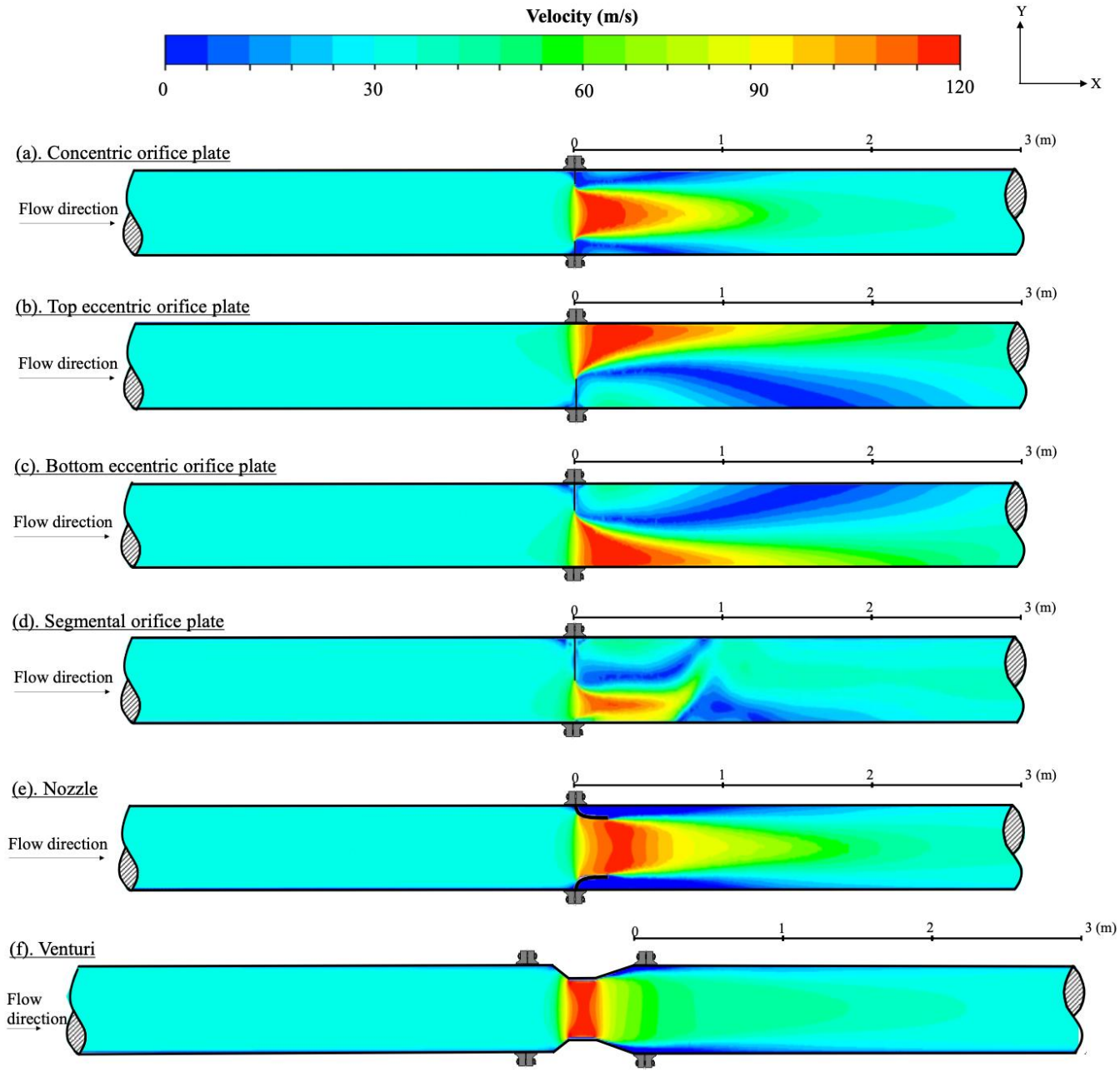


Figure 12. Velocity distributions for (a) concentric orifice, (b) top eccentric orifice, (c) bottom eccentric orifice, (d) segmental orifice, (e) Nozzle and (f) Venturi in vertical plane with inlet parameters $\dot{m}_g$=9.07 kg/s, $\dot{m}_f$=13.72 kg/s, h=1506.23 kJ/kg, x=39.82% (Mubarok et al., 2019).

An anomalous separated flow region occurs for the segmental orifice, where the high-velocity region is displaced to the upper part of the pipe 1 m downstream of the flange. This phenomenon may be due to a restriction plate with the height ($\bar{t}$) of 5 mm above the internal pipe wall. This simulated model uses a commonly manufactured design where the segmental orifice has the $\bar{t}$ (Liptak, 2003). Fig. 13 shows the velocity distribution comparison for two types of segmental orifice plate. This confirms that the restriction plate causes the unexpected flow separation on the bottom of the internal pipe wall (Fig. 12a), which is not found for the model without restriction (Fig. 13b).

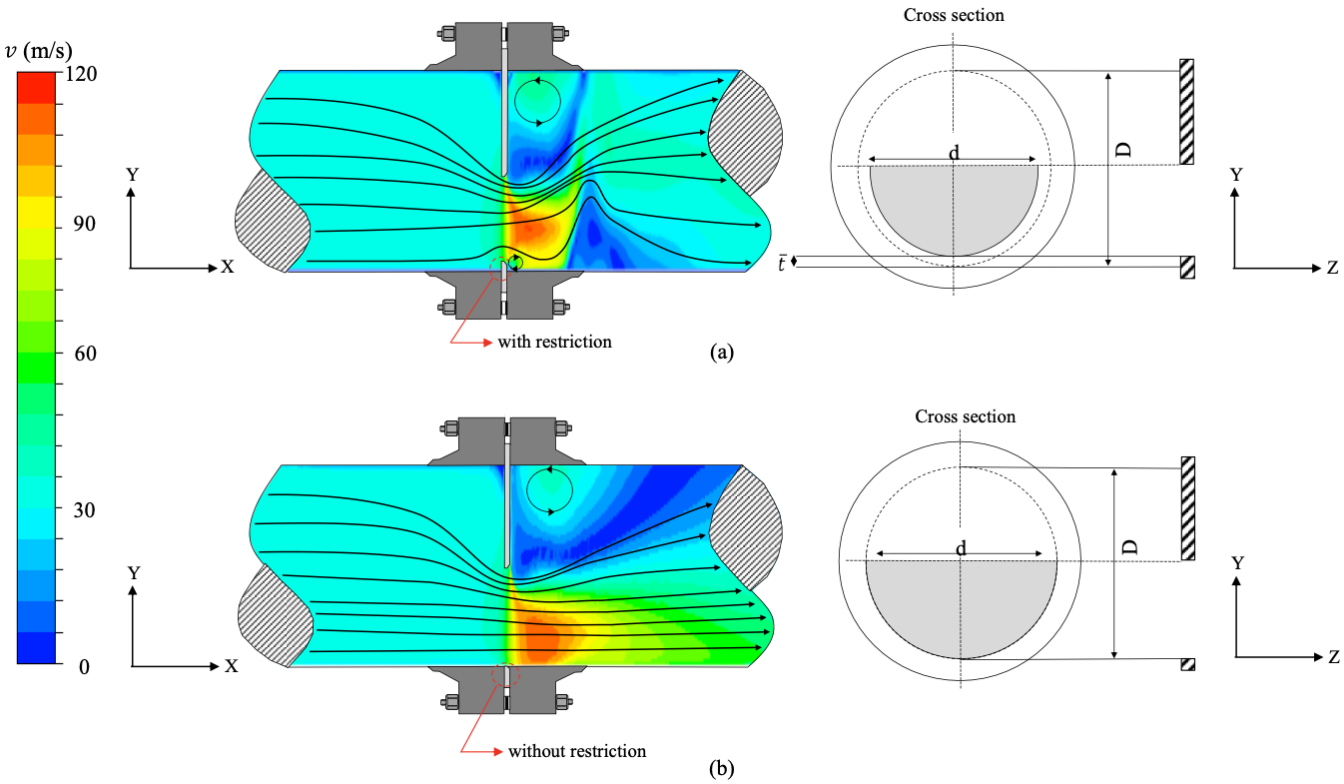


Figure 13. Velocity of two-phase flow through a segmental orifice meter in the vertical plane and central cross-section for model (a) with restriction and (b) without restriction (Mubarok et al., 2019).

7 CONCLUSIONS

Pressure differential devices are widely used in the geothermal industry to measure the mass flow rate of mainly single-phase fluid. Three-dimensional of geothermal two-phase flow through a concentric orifice plate has been simulated successfully by using CFD simulation technique using ANSYS-17.0 solver. The study has been investigated for two different turbulence models, realizable k-ε and SST k-ω. The results of both model simulations give very good agreement compared to experimental data of geothermal well UBL-A including pressure profile, velocity profiles and discharge coefficient. However, the SST k-ω model produced more accurate results than the realizable k-ε model based on the relative error values. Parameters setup of this model contribute to the achieve good results; mesh number, viscous turbulence model, pressure-velocity coupling method, spatial discretization, volume fraction courant number (Co) and pseudo time step.

Six different geometries of pressure differential flow meters – concentric orifice, top eccentric orifice, bottom eccentric orifice, segmental orifice, Nozzle and Venturi – were also investigated both experimentally and numerically for the measurement of two-phase geothermal fluid. The Venturi and Nozzle flow meters showed lower net pressure drops compared with the concentric orifice flow meter (87% and 67%, respectively. The low net pressure drops of the Venturi and the Nozzle flow meters are due to their elliptical restriction, which allows the fluid to flow through smoothly. The smallest net pressure drops among the flour orifice meters tested occurred with the segmental design, followed by the bottom eccentric, top eccentric and concentric orifice meters. The velocity profiles show identical flow distributions, with both increasing across the flow meters and reaching maximum values just downstream of the flow meter restriction. The highest turbulent kinetic energy occurs in the separation region, which formed between the velocity boundaries. In this case, the Venturi meter gives the lowest turbulent kinetic energy compared with the other flow meters. The shifting upward contours at downstream (X=1 m) in the segmental orifice are related to the bottom height restriction ($\bar{t}$) above the internal pipe.

Further CFD simulation analysis is needed to enhance the result of the models, especially to improve the pressure drop prediction. All the parameter's setup of this study can be used as a reference for further similar CFD model specifically for geothermal two-phase flow problems.

Acknowledgements

The author would like to thank PT Pertamina Geothermal Energy Tbk (PGE) for its support.

Nomenclature

A	Cross sectional area (m^2)
C	Orifice discharge coefficient
CFD	Computational fluid dynamics
Co	Courant number
D	Inside pipe diameter (m)
d	Orifice diameter (m)
DPM	Discrete phase model
D_ω	Cross-diffusion term
E	Orifice plate thickness (mm)
e	Sharp-edge orifice plate thickness (mm)
F_a	Orifice thermal expansion factor
F_C	Correlation factor
F_T	Time ratio correction factor
FEA	Finite element analysis
$\vec{F}$	Body force
G_b	Generation of kinetic energy due to buoyancy
G_k	Production of turbulence kinetic energy
G_ω	Generation of specific dissipation rate due to turbulence
$\vec{g}$	Gravity acceleration (m/s^2)
h	Enthalpy (kJ/kg)
K	Two-phase coefficient
k	Turbulence kinetic energy (m^2/s^2)
LRN	Low Reynolds number
$MFAT$	Ministry of foreign affairs and trade of New Zealand
$\dot{m}$	Mass flow rate of the fluid (kg/s)
PGE	Pertamina Geothermal Energy
p	Pressure (Pa)
p_1	Pressure upstream of the orifice plate (Pa)
p_2	Pressure downstream of the orifice plate (Pa)
$RANS$	Reynolds average Navier stokes
Re_D	Reynolds number for inner pipe diameter
RNG	Renormalization group
$SIMPLE$	Semi implicit pressure linked equation
SST	Shear stress transport
S_k, S_ω	User-defined source terms
UoA	The University of Auckland
U, V	Substitution factors to calculate orifice design coefficient
v, u	Fluid velocity (m/s)
$\vec{v}_m$	Averaged velocity (m/s)
$\vec{v}_{dr,k}$	Drift for secondary phase k
VoF	Volume of fluid
x	Dryness fraction of the fluid, variable in spatial derivative
Y_G	liquid compressibility coefficient
Y_k	Dissipation of turbulence kinetic energy due to turbulence
Y_M	Fluctuating dilatation effect to the overall dissipation rate
Y_ω	Dissipation of turbulence specific dissipation rate due to turbulence

Greek letters

Γ_k	Effective diffusivity of kinetic energy
Γ_ω	Effective diffusivity of specific dissipation rate
β	Rate of the orifice diameter to the inside pipe diameter ($\beta = d/D$)
ε	Turbulence dissipation rate (m^2/s^3)
μ	Dynamic viscosity (kg/ms)
ρ	Density (kg/m^3)
Δ_p	Differential pressure (Pa)
ω	Specific dissipation rate (1/s)

Subscripts

1Φ	Single-phase
2Φ	Two-phase
G	Gaseous/steam phase
H	Homogenous
i, j	Arbitrary i-th, j-th dimensions in spatial derivative
k	Arbitrary phase k
L	Liquid phase
m	Mixture phase
OP	Orifice plate

Superscripts

A	Cross sectional area (m^2)
a	Pressure coefficient of modified correlation
C	Orifice discharge coefficient
C_h	Enthalpy coefficient
D	Inside pipe diameter (m)
d	Orifice diameter (m)
F_a	Orifice thermal expansion factor
F_C	Correlation factor
F_T	Time ratio correction factor
K	Two-phase coefficient

REFERENCES

ANSYS. (2013). *ANSYS Fluent theory guide*. Canonsburg: ANSYS, Inc.

Bai, B., Zheng, X., 2017. Comparison of the two-phase mass flow coefficient and the over-reading for wet gas flow metering with DP meters. Exp. Therm. Fluid Sci. 90, 14–21.

Deendarlianto, Andrianto, M., Widyaparaga, A., Dinaryanto, O., Khasani, & Indarto. (2016). CFD Studies on the gas-liquid plug two-phase flow in a horizontal pipe. *Journal of Petroleum Science and Engineering*, 1-9.

Dehkordi, P.B., Colombo, L.P.M., Guilizzoni, M., Sotgia, G., 2017. CFD simulation with experimental validation of oil-water core-annular flows through Venturi and Nozzle flow meters. J. Pet. Sci. Eng. 149, 540–552.

Denton, G.S., 2009. CFD Simulation of highly transient flows. University College London.

Fadli, A. S., Karim, M. A., Harahap, R., & Taufik, A. (2015. *Pipeline failure analysis of bending pipe on the geothermal production well KMJ-X7 in Kamojang geothermal field, Indonesia*. Paper presented at the World Geothermal Congress 2015, Melbourne, Australia

Helbig, S., & Zarrouk, S. J. (2012). Measuring two-phase flow in geothermal pipelines using sharp edge orifice plates. *Geothermics, 44*, 52-64.

Hollingshead, C. L. (2011). *Discharge coefficient performance of venturi, standard cocentric orifice plate, v-cone, and wedge flow meters at small Reynolds numbers.* (Master Thesis), Utah State University, Utah, USA. (869)

James, R. (1965). Metering of steam-water two-phase flow by sharp-edged orifices. *Proceedings of the Institution of Mechanical Engineers, 180*(1), 549-572.

Jithish, K., & Kumar, P. A. (2015). Analysis of turbulent flow through an orifice meter using experimental and computational fluid dynamics simulation approach-A case study. *International Journal of Mechanical, 43*(4), 233-246. 10.1177/0306419015604432

Lin, Z. H. (1982). Two-phase flow measurements with sharp-edged orifices. *International Journal Multiphase Flow, 8*(6), 681-693.

Liptak, B.G., 2003. Instrument Engineers' Handbook: Process Measurement and Analysis, Volume I. ed. CRC Press, New York, USA.

Matsubara, C., Kuo, T., & Wu, H. (2013). Comparison of the effects of k-ϵ, k-ω, and zero equation models on characterization of turbulent permeability of porous media. *Journal of Water Resource and Hydraulic Engineering, 2*(2), 43-50.

Mazur, Z., Garcia-Illescas, R., & Porcayo-Calderon, J. (2009). Last stage blades failure analysis of a 28 MW geothermal turbine. *Engineering Failure Analysis, 16*, 1020-1032. 10.1016/j.engfailanal.2008.05.012.

Mubarok, M.H., Zarrouk, S.J., Cater, J.E., 2019. Comparative CFD modelling of pressure differential flow meters for measuring two-phase geothermal fluid flow. Geothermics 86, 101801.

Murdock, J. W. (1962). Two-phase flow measurement with orifices. *Journal of Basic Engineering, 84*(4), 419-432. 10.1115/1.3658657

Osato, K., Sato, M., & Kasai, K. (2016). *Coupled analysis using 3D-CFD and chemical model for corrosion and scaling of two-phase flow wellbore/pipeline.* Paper presented at the Proceedings 38th New Zealand Geothermal Workshop, Auckland, New Zealand.

Pointon, A. R., Mills, T. D., Seil, G. J., & Zhang, Q. (2009. *Computational fluid dynamic techniques for validating geothermal separator sizing*. Paper presented at the Geothermal Resource Council, Davis, USA

Purnanto, M. H., Zarrouk, S. J., & Cater, J. E. (2012). *CFD modelling of two-phase flow inside geothermal steam-water separators.* Paper presented at the New Zealand Geothermal Workshop Proceedings, Auckland, New Zealand.

Reader-Harris, M. (2015). *Orifice plates and venturi tubes*. In B. Wolfgang Merkirch, Germany, B. Donald Rockwell, USA & D. Cameron Tropea, Germany (Series Eds.). (pp. 393). doi:10.1007/978-3-319-16880-7

Roul, M. K., & Dash, S. K. (2012). Single phase and two-phase flow through thin and thick orifices in horizontal pipes. *Journal of Fluids Engineering, 134*, 1-14.

Shah, M. S., Joshi, J. B., Kalsi, A. S., Prasad, C. S. R., & Shukla, D. S. (2012). Analysis of flow through an orifice meter: CFD simulation. *Chemical Engineering Science, 71*, 300-309. 10.1016/j.ces2011.11.022

Siba, M. A., Mahmood, W. M. F., Nuawi, M. Z., Rasani, R., & Nassir, M. H. (2015). Modeling and applications of 3D flow in orifice plate at low turbulent Reynold Numbers. *International Journal of Mechanical & Mechatronics Engineering, 15*(4), 19-25.

Urner, G. (1997). Pressure loss of orifice plates according to ISO 5167-1. *Flow Measurement and Instrumentation, 8*, 39-41.

Versteeg, H. K., & Malalasekera, W. (1995). *An introduction to computational fluid dynamics, The finite volume method*. England: Longman Group Ltd.

Zahariea, D. (2016. *Numerical analysis of eccentric orifice plate using ANSYS Fluent software*. Paper presented at the 20th Innovative Manufacturing Engineering and Energy Conference,

Zarrouk, S. J., & Purnanto, M. H. (2014). Geothermal steam-water separators: design overview. *Geothermics, 53*, 236-254.

Zhang, H. J., Lu, S. J., & Yu, G. Z. (1992). An investigation of two-phase flow measurement with orifices for low-quality mixtures. *International Journal Multiphase Flow, 18*(1), 149-155.